Science Advances
AAAS

Manuscript Template

This manuscript had been first submitted for publication on December 9, 2022, and then resubmitted on August 3, 2023.

FRONT MATTER

Title

- A thermally-conductive Martian core and implications for its dynamo cessation
- Mars' thermally-conductive core and dynamo cessation

Authors

Wen-Pin Hsieh[1,2]*, Frédéric Deschamps[1]*, Yi-Chi Tsao[1], Takashi Yoshino[3], and Jung-Fu Lin[4]

Affiliations

[1]*Institute of Earth Sciences, Academia Sinica, Taipei 11529, Taiwan*

[2]*Department of Geosciences, National Taiwan University, Taipei 10617, Taiwan*

[3]*Institute for Planetary Materials, Okayama University, Misasa 682-0193, Japan*

[4]*Department of Geological Sciences, Jackson School of Geosciences, University of Texas at Austin, Austin, Texas 78712-0254, USA*

Correspondence: W.P.H. (wphsieh@earth.sinica.edu.tw) and F.D. (frederic@earth.sinica.edu.tw).

Abstract

Mars experienced a dynamo process that generated a global magnetic field ~4.3–3.6 Ga. The cessation of this dynamo strongly impacted Mars' history and is expected to be linked to thermochemical evolution of Mars' iron-rich liquid core, which is strongly influenced by its thermal conductivity. Here we directly measured thermal conductivities of solid iron-sulfur alloys to pressures relevant to the Martian core and temperatures to 1023 K. Our results show that a Martian core with 16 wt% sulfur has a thermal conductivity of ~19 to 32 W m^{-1} K^{-1} from its top to the center, much higher than previously inferred from electrical resistivity measurements. Our modelled thermal conductivity profile throughout the Martian deep-mantle and core indicates a ~4 to 6-fold discontinuity across the core-mantle-boundary. The core's efficient cooling resulting from the depth-dependent, high conductivity diminishes thermal convection and forms thermal stratification, significantly contributing to cessation of Martian dynamo.

Teaser

Mars' core is much more thermally-conductive than previously inferred, which critically contributes to stop its early dynamo.

MAIN TEXT

Introduction

Thermal conductivity of rocky planets' cores controls their thermal evolution and dynamics, which drive and maintain the dynamo action and magnetic fields of these planets (*1–3*). Convection of an iron (Fe)-rich liquid core is predominantly operated by thermal and compositional buoyancy (*4–7*). Thermal buoyancy is produced as the super-isentropic heat flux extracted across the core-mantle-boundary (CMB) to the mantle is larger than a minimum value. The compositional buoyancy, on the other hand, is generated by a gravitationally unstable density distribution via either phase transition (e.g., crystallization of the liquid core), or exsolution of materials and immiscibility of elements (*8–10*). Interestingly, the evolution history of the dynamo and magnetic fields of Mars are strikingly different from those of the Earth: satellites magnetic data on the Martian crustal rocks suggested an early, short-lived dynamo that once operated ~4.3–3.6 Ga (see, e.g., Ref (*11–14*) for details of the dynamo history), while the Earth's dynamo, predominantly powered by inner core crystallization, remains active today. Paleomagnetic data (*15*) suggested that Earth's dynamo slowly decayed from 2.5 to 0.5 Ga, but recovered as the inner core started to grow. Hemingway and Driscoll (*16*) suggested that Martian dynamo may be intermittent. They showed that the presence of a solid inner core in Mars is compatible with the absence of a present-day dynamo, and that a compositionally powered dynamo could become effective in the next ~1 Gyrs. Note, however, that InSight data suggested that Martian core is entirely molten and lighter than expected (*17*), indicating that it may be richer in light elements. Finally, it is worth pointing out that Mercury, which is smaller than Mars but has an inner core, has a faint magnetic field triggered by a core dynamo, while Venus, whose size is similar to Earth, does not. These suggest that the size of a planet is not the primary parameter controlling the presence of dynamo, and that other aspects, including core composition and its effects on physical properties, play crucial roles in maintaining a dynamo. Martian core's thermal conductivity holds

a key to estimate the available thermal and compositional energy to operate its dynamo, and thus to reconstruct its thermochemical history. Recent numerical simulations (*1*) explored the influence of thermal conductivity on core evolution by doing a systematic parameter survey over a broad range of potential thermal conductivity values and revealed that a high core thermal conductivity (16–35 W m^{-1} K^{-1}) could be a critical factor to cease its global magnetic field. The assumption that thermal conductivity at Martian core's condition is high has, however, never been experimentally verified.

Recent seismic observations by the InSight lander (*17*) and the geodetic data inferred a liquid Martian core that is larger than previously expected. Furthermore, it is implied that the entire Martian mantle has a mineralogy similar to that in the Earth's upper mantle and transition zone, i.e., ringwoodite is the major mineral in Martian deep mantle, while bridgmanite, the predominant mineral in Earth's lower mantle, is not present within Mars. Given the limited cosmochemical and geophysical data as well as different model assumptions, the composition of the Martian core remains poorly constrained (see Ref (*18, 19*) and references therein). However, it is commonly considered to be made of Fe alloyed with significant amounts of light elements, including sulfur (S) as the major one, along with small amounts of oxygen (O), carbon (C), and hydrogen (H). Due to the abundance and siderophile characteristic of S, its proposed content in the Martian core typically falls in the range of ~10–25 wt% (*18–20*). This motivates us to choose, for simplicity, eutectic Fe_3S (~16 wt%) and FeS (~36 wt%) as representative compositions, and to study their thermal conductivity at Martian core pressure-temperature (*P*-*T*) conditions, providing pivotal insights to their impacts on the fate of Martian dynamo.

The heat flux across the Martian CMB, Q_c, is crucial for determining the evolution of the thermal state and dynamo action in the Martian core. This flux is controlled by heat transfer through the mantle, which itself depends on the lowermost mantle thermal conductivity, as it controls the conductive heat transfer through thermal boundary layers, as well as on the efficiency

of mantle convection (if happening at all). The lowermost mantle thermal conductivity may be estimated from mineral physics measurements of ringwoodite's thermal conductivity (*21*). On the core side, heat transfer and dissipation, which play a crucial role on the core and dynamo evolutions, depend on the core's thermal conductivity. The thermal conductivity of Fe-S alloys may bring important constraints on this conductivity, but has never been directly measured under Martian core's high *P-T* conditions. Previous studies have largely focused on the determination of the electrical resistivity ρ of Fe-S alloys, which is then used to infer its thermal conductivity through the Wiedemann-Franz (WF) law with ideal Lorenz number (see, e.g., Ref (*22*) and references therein). First-principles theoretical calculations showed that at Martian core conditions the ρ of liquid Fe_3S and Fe_7S remains at ~107 μΩ cm and ~88 μΩ cm, respectively (*23*); these results infer a relatively high Martian core's thermal conductivity (~50 W m^{-1} K^{-1}). Note that with similar approaches, Earth's core thermal conductivity was inferred to be ~80–300 W m^{-1} K^{-1} (*22*). Experimental high *P-T* measurements on the ρ of solid Fe-S alloys were, however, typically limited to ≦10 GPa (*24–26*). Extrapolation of such low-pressure data to Martian core's high-pressure conditions (~18–40 GPa) suggested a low thermal conductivity of ~10 W m^{-1} K^{-1} in Martian core. These contradictory results lead to distinct implications for the energy budget of the Martian core and Q_c, and different scenarios for the evolution of the dynamo. Since the validity of applying the WF law with ideal Lorenz number on the Fe-light element alloys (e.g., Fe-S alloys) under extreme conditions remains uncertain and is being challenged (*2*), direct and precise determination of their thermal conductivity at high *P-T* conditions relevant to the Martian core is key to constrain its thermal conductivity and understand the mechanisms that stop its dynamo.

In this work, our direct high *P-T* thermal conductivity measurements of Fe-S alloys combined with data modeling allow us to build a depth-dependent thermal conductivity profile from the Martian deep-mantle to its core, providing the first direct experimental evidence for a

highly thermally-conductive Martian core. Such high thermal conductivity enables efficient cooling of the Martian core and formation of thermal stratification layer, leading to a short-lived (~0.5–0.8 Gyr) dynamo that ceased ~4 Gyr ago.

Results

Thermal conductivity at high pressure and room temperature

We used time-domain thermoreflectance (TDTR) coupled with diamond anvil cell (DAC) (*2*, *27*, *28*) (see Methods) to precisely measure the thermal conductivity of polycrystalline Fe_3S and FeS to ~40 GPa at room temperature. We find that the thermal conductivity of Fe_3S (~16 wt% S) at ambient conditions is ~6.8 W m^{-1} K^{-1} (Fig. 1(a)), which is more than an order of magnitude smaller than that of pure Fe (~76 W m^{-1} K^{-1}) (*2*), indicating a strong reduction of thermal conductivity caused by the sulfur impurity. Application of pressure monotonically enhances the thermal conductivity, which reaches ~25 W m^{-1} K^{-1} at 40.5 GPa, the pressure at the center of the Mars. Moreover, with ~36 wt% S impurity, the FeS shows drastically distinct values of thermal conductivity and pressure dependence (Fig. 1(b)). The thermal conductivity of FeS at ambient conditions (FeS I phase) is even lower than that of Fe_3S, down to ~2.9 W m^{-1} K^{-1}. Upon compression across ~3.4 GPa, the thermal conductivity suddenly increases to 9 W m^{-1} K^{-1} at 5.2 GPa (FeS II phase). After the transition at ~6.7 GPa to FeS III phase, considering the data uncertainty, the thermal conductivity remains approximately at 7.5 W m^{-1} K^{-1} until ~25 GPa, after which it significantly increases to 12 W m^{-1} K^{-1} at 43 GPa, half of the Fe_3S at similar pressures.

It's worth noting that, similar to the effect of silicon alloying (*2*), presence of ~16 wt% (Fe_3S) and ~36 wt% S (FeS) in Fe significantly reduces the thermal conductivity, presumably due to the strong inelastic scattering between electrons and impurities (*29*–*31*). The impurity effects also alter the pressure dependences of Fe_3S and FeS, which are considerably different from that of pure Fe, where a concave pressure dependence with a minimum at ~40 GPa was observed (*2*).

Thermal conductivity at high pressure-temperature conditions

To quantify the effects of temperature and sulfur alloying, we further performed high *P*-*T* thermal conductivity measurements on the Fe_3S and FeS in externally-heated DACs (Fig. 2). The thermal conductivities of Fe_3S and FeS both increase with temperature, similar, again, to the behaviors of Fe-Si alloys (*2*, *32*). Note that along the *P*-*T* path of our measurements (i.e., first compressing the sample to a fixed pressure and then raising the temperature), the Fe_3S stayed in the tetragonal structure (*33*), while the FeS transitioned from FeS III to IV phase at ~730 K (*34*). Though our measurement temperature was only up to ~1023 K, we observed clear temperature dependences that change with the pressure and S content. We should note that the estimated Martian core temperature was ~2000–2400 K (*35*). If we assume the thermal conductivity can be phenomenologically modelled as $\Lambda(T) = aT^n$, where a is a normalization constant, the exponent value n can be determined by the linear slope in the $\ln\Lambda$-$\ln T$ plot. Interestingly, for Fe_3S, $n = 0.25$ (±0.07) at 15.4 GPa and slightly decreases with pressure to $n = 0.2$ (±0.04) at 35.5 GPa (Fig. 2(a)). With higher content of S impurity that results in stronger carrier scattering, the FeS IV phase has a stronger temperature dependence than the Fe_3S at similar pressures: $n = 0.36$ (±0.07) at 27 GPa and $n = 0.33$ (±0.05) at 28 GPa, respectively (Fig. 2(b)). Though the crystal structure of Fe_3S and FeS is different, our results suggest that at a given pressure, the higher content of impurity would have a stronger temperature dependence, which has also been reported in Fe-Si alloys (*2*, *32*) (see discussion).

Discussion and implications for the Martian dynamo evolution

Temperature dependence of thermal conductivity

The Wiedemann-Franz (WF) law relates the electronic thermal conductivity Λ_e of a material with its electrical resistivity ρ by $\Lambda_e = L \times T/\rho$, where L is the Lorenz number that may vary with pressure and temperature, and T the absolute temperature. Typically, when the temperature is

comparable or higher than the Debye temperature of the material, its electrical resistivity can be expressed approximately as $\rho = \rho_0+\alpha+\beta T$, where ρ_0 is the residual resistivity arisen from defect-scattering, α a phenomenological constant associated with the shift in the resistivity due to temperature effect, and β a temperature coefficient (*36*, *37*). Therefore, Λ_e can be rewritten as $\Lambda_e \sim L\times T/(\rho_0 + \alpha + \beta T)$. Since our measurement temperature (300–1023 K) is higher than 1/3 of the Debye temperature of Fe-S alloys (~ 400 K) (*38*), the high contents of S impurity in Fe makes the sum of ($\rho_0 + \alpha$) larger than βT (*37*). The Λ_e of F-S alloys is thus expected to increase with increasing temperature. Furthermore, with increasing S content, the relative contribution of βT to the total electrical resistivity would be further reduced, leading to a stronger temperature dependence. On the other hand, for both Fe_3S and FeS, the temperature exponent n decreases with pressure, in line with the general trend observed for the $Fe_{0.85}Si_{0.15}$ (*2*). This is presumably caused by the fact that pressure reduces the effective density of impurity in momentum space (less impurity-scattering) and enhances the relative contribution of βT, leading to a weaker temperature dependence of thermal conductivity (*36*).

Thermal conductivity profiles in Martian core and mantle

The recent geophysical observations by the InSight mission (*17*) suggest that the Martian core is larger than previously thought and confirm that, by contrast to the Earth, the Martian mantle is too thin to allow a transition from ringwoodite to bridgmanite, i.e., ringwoodite is the major mineral in its deep mantle. The mean Martian core density derived from InSight observations spans from ~5.7–6.3 g cm^{-3}, where a number of potential combinations of S, O, and H contents alloyed in an Fe-Ni core is discussed (*17*). Geochemically defensible amounts of these light elements with a mean core density >6 g cm^{-3} are at the upper end of such density range. With a lower bulk mantle FeO content, the Insight observations preliminarily suggests that the core is majorly composed of Fe-Ni along with ~10–15 wt% S, <5 wt% O, and <1 wt% H and C (*17*). To

197 understand the thermal evolution history of Mars and its early dynamo, we first model the thermal
198 conductivity of the Martian core and mantle along an estimated Martian areotherm taken from
199 Ref (*35*) (an estimated present-day radial temperature profile within Mars), based on our present
200 high *P*-*T* thermal conductivity of solid Fe-S alloys and previous data for ringwoodite (*21*). Note
201 that if the core temperature were as high as 3000 K early in Mars' history, our modelled thermal
202 conductivity of Martian core would be increased by only ~6%, which is within our data
203 uncertainty. In other words, the temporal changes in the Martian areotherm as it cools down since
204 its early stage have minor effects on our modelled thermal conductivity and numerical simulations
205 on its thermal evolution. For the solid Fe_3S and FeS, we assume their temperature dependences of
206 thermal conductivity at Martian core *P*-*T* conditions follow those shown in Fig. 2, i.e., scaling
207 with $T^{0.21}$ and $T^{0.33}$, respectively. The thermal conductivity of ringwoodite, on the other hand, is
208 assumed to follow a $T^{-0.5}$ dependence, typical of Fe-bearing minerals (*27*, *39*–*41*). The modelled
209 thermal conductivities of ringwoodite (blue curves), solid Fe_3S (black curve), and solid FeS
210 (orange curve) along a Martian areotherm are plotted in Fig. 3.

211 Literature experimental investigations on the high *P*-*T* electrical resistivity ρ of solid Fe-S
212 alloys have been largely limited to ≦10 GPa (*24*–*26*). For instance, ρ of Fe-20wt%S at 4.5 GPa
213 was found to be ~400 μΩ cm up to ~1400 K (*24*), and ρ of FeS at 5 GPa (*26*) and 8 GPa (*24*)
214 remained at ~400 μΩ cm and ~700 μΩ cm, respectively, up to ~1700 K. Their corresponding
215 thermal conductivities were then further inferred to be ~6–11 W m^{-1} K^{-1} via the WF law with an
216 ideal Lorenz number. In addition, based on high pressure but room temperature electrical
217 resistivity measurements, ρ of solid Fe-14.2wt%S at Martian core conditions was estimated to
218 ~100 μΩ cm, suggesting a thermal conductivity of 46 W m^{-1} K^{-1} at the Martian CMB and 62 W m^{-1} K^{-1}
219 at the center (*42*). Using first-principles calculations, ρ of liquid Fe_3S and Fe_7S were
220 determined to stay at ~107 μΩ cm and ~88 μΩ cm, respectively, throughout the Martian core
221 conditions (*23*). Again, it is important to note that our present study represents the first direct high

P-T thermal conductivity measurements of solid Fe-S alloys that do not rely on the WF law and assumption of ideal Lorenz number. Our results for the thermal conductivities of solid Fe-S alloys (solid black and orange curves in Fig. 3) under similar *P-T* conditions and S content are much higher than those inferred from high *P-T* experimental electrical resistivity data (*24*), while only about half of those estimated from room temperature resistivity data (*42*) and calculated by first-principles (for liquid phase) (*23*). Table 1 summarizes thermal conductivity of Fe-S alloys at Martian CMB conditions. Here we only include literature results available at CMB *P-T* conditions with an S content similar to our present study, as the chemical composition could significantly influence the thermal conductivity of Fe alloys.

Moreover, prior studies have suggested that the effect of melting would reduce the thermal conductivity of Fe and Fe alloys by ~20% or less (see, e.g., Ref. (*2*) and references therein). Assuming S is the major light element with ~16 wt% (~25 at%) (*20*) in the Martian core and a 15% conductivity reduction upon melting, our present data suggest that the thermal conductivity of liquid Fe_3S (red dashed curve in Fig. 3) would be ~19 W m^{-1} K^{-1} at the top of the Martian core, and that it increases by ~70% to ~32 W m^{-1} K^{-1} at the center, leading to a much more thermally-conductive Martian core than previously inferred. In addition, if the mineralogy of the Martian mantle is similar to that of the Earth's upper mantle, which is predominantly composed of olivine and its high-pressure polymorph ringwoodite, the thermal conductivity of ringwoodite in dry phase at the bottom of the mantle would be ~4.5 W m^{-1} K^{-1} (blue solid curve in Fig. 3). Note that if the ringwoodite in the Martian mantle contains substantial amounts of water, its thermal conductivity would be lower. For instance, the presence of 1.73 wt% water would lead to a conductivity of ~3 W m^{-1} K^{-1} at the bottom of the Martian mantle (see the blue dashed curve). Furthermore, if the ringwoodite in the Martian mantle contains more iron than that in the Earth, its thermal conductivity would be even lower. Overall, a ~4 to 6-fold thermal conductivity discontinuity is expected across the Martian CMB (liquid Fe_3S vs. ringwoodite), which would

suppress heat released from the core and promote thermal stratification. Such findings yield distinct behaviors concerning the Q_c (see geodynamic modeling below). In addition, our results for Fe_3S and FeS at Martian core's *P-T* conditions provide a platform to model the thermal conductivity of the Fe-S alloys with different S contents, since under different model assumptions the not-well-constrained S content in the Martian core may vary over the range we explored (~16–36 wt%) during Mars history. If the Martian core also contains few amounts of other elements (e.g., O, H, and C, etc.), these impurities are expected to further slightly reduce the thermal conductivity of Martian core, while their exact effects require future experimental and computational studies.

Implications for Martian thermal evolution and dynamo cessation

Dynamo operation and duration strongly depend on core thermal conductivity. Higher thermal conductivity promotes faster dynamo decay through ohmic dissipation, and in absence of gravitational energy released from core crystallization the dynamo may rapidly switch off. Recent simulations of Mars core-mantle coupled evolution (*1*) indicate that the cessation time of the Martian magnetic field (*11–13*) can be explained with a core thermal conductivity in the range of 16–35 W m^{-1} K^{-1}, provided that the mantle reference viscosity, η_0, is between 10^{19} and 10^{21} Pa s. Modelling details further show that the pressure dependence of mantle viscosity (with an activation volume fixed to 6 cm^3 mol^{-1}) requires a lower range of reference viscosity (10^{19}–10^{20} Pa s) and thermal conductivity (< 20 W m^{-1} K^{-1}) to explain this cessation time.

Here we investigate how the radial profile of the core thermal conductivity, Λ_c (red dashed curve in Fig. 3), impacts Mars thermal evolution. For this, we performed simulations coupling parameterized models of core and mantle evolution following the method developed in Ref (*1*) (also see method section), with the exception that the thermal conductivity is now allowed to vary with depth. Figure 4 plots evolution of key parameters ((a) heat flow Q_c, (b) entropy arising from

ohmic dissipation, E_j, (c) bottom radius of the thermally stratified layer, r_s, and (d) temperature at the CMB) for three different scenarios, including the reference case in Ref (*1*) (green curves). Thermal stratification is a consequence of a sub-isentropic heat flow (i.e., Q_c is lower than the heat flow along an isentropic temperature gradient, Q_a), and results in higher core temperatures. All cases were performed with the "standard" configuration of Ref (*1*), i.e., the mantle viscosity does not depend on pressure (activation volume is set to zero), and the mantle abundance in heat-producing elements is that of Ref (*43*). In addition, the initial mantle temperature and temperature jump at the CMB were set to 2327 K and 182 K, respectively, corresponding to the standard reference case in Ref (*1*), and leading to an initial CMB temperature of 2509 K. Dynamo switches off when E_j is below a small value $E_{j,min}$, corresponding to the minimum ohmic dissipation needed to self-sustain feedbacks between magnetohydrodynamic processes. For Earth, and in the case of a poloidal field, this value was estimated to 1.0 MW K^{-1} (*44*), which we adopted in our estimation of the Martian dynamo cessation time. Greenwood et al. (*1*) pointed out that because $E_{j,min}$ is much smaller than the dissipation provided by secular cooling, its exact value does not substantially influence the dynamo cessation time. The condition $E_j < 1.0$ MW K^{-1} occurs around the transition from super- to sub-isentropic heat flow (i.e., Q_c being slightly higher or lower than Q_a). For the reference case (Λ_c is a constant of 24 W m^{-1} K^{-1} throughout the core and $\eta_0 = 2.5\times10^{20}$ Pa s; green curves in Fig. 4), this happens ~0.9 Gyr, well within the estimated cessation range (*11–13*). For the depth-dependent profile of Λ_c based on our experimental data and still with $\eta_0 = 2.5\times10^{20}$ Pa s, dynamo cessation occurs later, ~1.1 Gyr (blue curves in Fig. 4). Within error bars (blue shaded area), however, the cessation time expected from our Λ_c profile agrees with the observed range. In addition, good agreement can be obtained by assuming a slightly higher mantle viscosity (red curves in Fig. 4, the same Λ_c profile as the blue curves, but with $\eta_0 = 3.5\times10^{20}$ Pa s). Thermal stratification starts when Q_c becomes lower than Q_a. Our calculations indicate that Q_a is lower with depth-increasing conductivity, which delays the onset of

stratification. For the reference case, stratification starts ~0.3 Gyr before dynamo cessation, while it starts ~0.4–0.6 Gyr after dynamo cessation when the depth-dependent Λ_c is accounted for. Moreover, core thermal stratification is much faster with the depth-dependent Λ_c. For instance, the entire core is thermally stratified by 2.8 Gyr with our Λ_c profile and $\eta_0 = 2.5\times10^{20}$ Pa s (blue curve in Fig. 4(c)), compared to ~4.5 Gyr for the reference case (green curve). A possible explanation for this faster stratification is that, compared to the constant Λ_c case, due to the depth-increasing Λ_c, the increase in cooling rate of the convecting core is greater than that of the stable layer, meaning the thermal stratification completes earlier.

One aspect that is not accounted for in our simulations is the possible presence of a basal layer enriched in iron and heat producing elements at the base of the mantle (*45*). Such a layer may result from the crystallization of Martian magma ocean, and is expected to be partially molten due to high temperatures in the CMB region, and to transfer heat by conduction. Because it is partially molten and enriched in iron, one would further expect the thermal conductivity of this layer to be much lower than that of ringwoodite (blue curve in Fig. 3). In other words, if such a layer exists, it would act as a thermal blanket, opposing core cooling and dynamo action. Combined with our present core thermal conductivity, it would, in turn, request a lower mantle viscosity to explain the observed dynamo cessation time. Future direct measurements and computational studies on the thermal conductivity of other Fe-S-light element systems under relevant *P*-*T* conditions are required to better constrain the thermal evolution and energy budget of the Mars.

Materials and Methods

Starting materials and sample preparation

The Fe_3S polycrystals were synthesized by a Kawai apparatus with a 5000 ton press (run number 5K3187). The starting material is a powder mixture of Fe and S with an atomic ratio of

3:1. The sample was compressed to 22 GPa, and first heated to 1000˚C, followed by a cooling process from 1000˚C to 855˚C for 9.5 hrs, and finally kept at 700˚C for 2hrs. The starting FeS troilite powder was extracted from the Cape York IIIAB iron meteorite, also known as the Innaanganeq meteorite, in the Geological Museum of the University of Copenhagen, Denmark. Troilite in iron meteorites is known to be very chemically stoichiometric FeS, which is more suitable for the present study than commercial pyrrhotite samples ($Fe_{1-X}S$) with iron deficiency (X = 0 to 0.2). The chemical composition of Fe_3S and FeS was characterized to be $Fe_{2.97}S$ (with a small amount of Fe_3S_2) and $Fe_{0.995}S$, respectively, by electron probe microanalyzer in Academia Sinica.

To prepare samples for thermal conductivity measurements at high pressure and room temperature, each sample was firstly hand-polished down to ~10 μm thick, and then thermally evaporated with a 90 nm thick Al film. The sample along with several ruby spheres was loaded into a symmetric diamond anvil cell (DAC) where a pair of 300 μm culet anvils and a Re gasket were used. Due to its relatively low thermal conductivity at high pressures, silicone oil (CAS No. 63148-62-9 from ACROS ORGANICS) was loaded as the pressure transmitting medium, which remains in a reasonably well quasi-hydrostatic condition over the pressure range we studied (<45 GPa). The pressure within the sample chamber of the DAC was monitored by fluorescence(*46*) and Raman of the ruby with a typical uncertainty of <5%.

In our high *P-T* measurements, the ~10 μm-thick sample and ruby spheres were loaded into an externally-heated DAC (EHDAC). Here polycrystalline NaCl powder (thermally dried at ~120℃ for one hour before being loaded) was used as the pressure medium. The EHDAC provides a spatially homogeneous temperature distribution over the sample chamber. Since the pressure within the sample chamber may change upon heating, a gas membrane that enables *in situ* control on the pressure within the EHDAC was also used. The combination of these techniques allows us to investigate the temperature dependence of thermal conductivity of Fe_3S

and FeS at a given pressure up to ~1023 K. Details of the EHDAC assemblage and pressure-temperature measurement, as well as the sample geometry and experimental setup can be found in Ref (*39*, *47*).

Thermal conductivity measurements

We used time-domain thermoreflectance (TDTR) to measure the thermal conductivity of Fe_3S and FeS over a wide range of *P-T* conditions presented in this work. TDTR is a widely used thermal metrology method that provides thermal conductivity measurements of various materials with high precision. In the past decade, it has also been successfully coupled with high *P-T* techniques, see, e.g., Ref (*2*, *27*, *39*, *48*). In short, TDTR is an ultrafast optical pump-probe spectroscopy, which uses a split pump pulse to heat up the Al film coated on the sample, and a split probe pulse to detect the heat diffusion dynamics through the sample. By comparing the temporal evolution of the Al's reflectivity change with numerical calculations based on a bi-directional thermal model, the thermal conductivity of the sample of interest is determined. More details of the principle, experimental setup, and data analysis of the TDTR are described in literatures, e.g., Ref (*2*, *47*–*50*) and references therein.

Supplementary Materials Fig. S1 shows a set of representative TDTR spectrum for Fe_3S at 40.5 GPa and room temperature along with data fitting by the thermal model calculations. In the thermal model, the volumetric heat capacity of the sample of interest (Fe-S alloys) is an important parameter. At ambient conditions, the volumetric heat capacity of FeS is 2.78 J cm^{-3} K^{-1} taken from Ref (*51*), while that of Fe_3S is estimated to be 3.16 J cm^{-3} K^{-1} by linear interpolation between pure Fe (3.54 J cm^{-3} K^{-1}) and FeS. The heat capacity of both FeS and Fe_3S at high *P-T* conditions are not known, and thus assumed to be a constant as their ambient values. We note that the uncertainty in our data majorly arises from the analysis uncertainty, rather than the measurement uncertainty. Based on the method (*52*, *53*) described in Supplementary Materials Fig. S1 and S2,

the uncertainties in all the parameters in our thermal model calculations would translate <10% error in the derived thermal conductivity of Fe-S alloys before 20 GPa, and ~10–17% error at 20–40 GPa.

Modelling of core evolution

To investigate the evolution of the Martian core, including the growth of a stable layer, and to estimate the cessation time of Martian dynamo, we used the approach in Ref (*1*), which is coupling models of parameterized convection for the core and for the mantle.

For the mantle, this approach uses a parameterization based on stagnant lid thermal convection (*54*, *55*) with a simplified lithosphere. The mantle is heated both from below (heat extracted from the core) and from within (radiogenic heating due to the decay of U, Th and K). Concentration in heat producing elements is taken from the compositional model of Ref (*43*). The convective interior is assumed isothermal, and temperature increases linearly with depth within thermal boundary layers. The crust thickness is considered as constant over time, and melting and crust growth are neglected. The thickness of the stagnant lid (modelling the lithosphere) is set to 300 km. Ref (*1*) showed that the thickness of the stagnant lid does not have a strong impact on the evolution of the mantle convective interior and of the core. Mantle viscosity depends on temperature following an Arrhenius law with activation energy fixed to 300 kJ mol^{-1}, and is specified (reference viscosity η_0) at a temperature of 1600 K. Viscosity is further allowed to increase with temperature, but, for simplicity, here is neglected this dependence (activation volume V_a is set to 0). The time for dynamo's cessation strongly depends on η_0 and, to a lesser extent on activation volume (*1*). For core thermal conductivity in the range of 16-35 W m^{-1} K^{-1}, calculated cessation time agrees with that estimated for Martian dynamo with viscosity in the range of 10^{20}-10^{21} Pa s. Accounting for viscosity pressure dependence (V_a=6 cm^3 mol^{-1}) reduces

this range by one order of magnitude. In calculations, we tested values of the reference viscosity, $\eta_0=2.5\times10^{20}$ Pa s and $\eta_0=3.5\times10^{20}$ Pa s.

The core is initially well mixed with an adiabatic temperature profile and is animated with convection. The core is initially assumed super-heated compared to the mantle with a temperature difference dT, which we fixed to 182 K, based on the standard model from Ref (*1*) , and the temperature at the CMB is re-adjusted according to this treatment. The heat flow at CMB, Q_c, is calculated from scaling relationships built for mantle convection (*55*) and is further depending on the temperature at the CMB, T_{CMB}, which is determined from the core evolution. As Q_c becomes lower than the heat flow calculated along an isentropic temperature profile, Q_a, a stable conductive layer starts to grow and core convection is confined beneath this layer. The evolution of the stable layer follows the treatment in Ref (*56*). The ohmic dissipation related to magnetic field is measured with the entropy balance E_j between the entropies originating from secular cooling and thermal conduction, E_s and E_k, which are calculated following Ref (*56*). Because E_k is proportional to the core thermal conductivity, Λ_c, larger conductivity leads to larger E_k and thus lower E_j. In other words, dynamo action is reduced with increasing Λ_c and may stop if conduction is too large.

References

1. S. Greenwood, C. J. Davies, A. Pommier, *Geophys. Res. Lett.*, **48**, e2021GL095198 (2021).
2. W.-P. Hsieh, A. F. Goncharov, S. Labrosse, N. Holtgrewe, S. S. Lobanov, I. Chuvashova, F. Deschamps, J. Lin, Low thermal conductivity of iron-silicon alloys at Earth's core conditions with implications for the geodynamo. *Nat. Commun.* **11**, 3332 (2020).
3. K. Hirose, S. Labrosse, J. Hernlund, Composition and State of the Core. *Annu. Rev. Earth Planet. Sci.* **41**, 657 (2013).
4. J. P. Williams, F. Nimmo, Thermal evolution of the Martian core: Implications for an early dynamo. *Geology*. **32**, 97–100 (2004).
5. C. J. Davies, A. Pommier, Iron snow in the Martian core? *Earth Planet. Sci. Lett.* **481**, 189–200 (2018).
6. B. A. Buffett, The Thermal State of Earth ' s Core. *Science*. **299**, 1675–1677 (2003).

7. S. Labrosse, Thermal and magnetic evolution of the Earth's core. *Phys. Earth Planet. Inter.* **140**, 127–143 (2003).

8. J. Badro, J. Siebert, F. Nimmo, An early geodynamo driven by exsolution of mantle components from Earth's core. *Nature*. **536**, 326–328 (2016).

9. J. G. O'Rourke, D. J. Stevenson, Powering Earth's dynamo with magnesium precipitation from the core. *Nature*. **529**, 387–389 (2016).

10. S. Yokoo, K. Hirose, S. Tagawa, G. Morard, Y. Ohishi, Stratification in planetary cores by liquid immiscibility in Fe-S-H. *Nat. Commun.* **13**, 644 (2022).

11. M. H. Acuña, J. E. P. Connerney, N. F. Ness, R. P. Lin, D. Mitchell, C. W. Carlson, J. McFadden, K. A. Anderson, H. Rème, C. Mazelle, D. Vignes, P. Wasilewski, P. Cloutier, Global distribution of crustal magnetization discovered by the Mars Global Surveyor MAG/ER experiment. *Science*. **284**, 790–793 (1999).

12. B. Langlais, E. Thébault, A. Houliez, M. E. Purucker, R. J. Lillis, A New Model of the Crustal Magnetic Field of Mars Using MGS and MAVEN. *J. Geophys. Res. Planets*. **124**, 1542–1569 (2019).

13. A. Mittelholz, C. L. Johnson, J. M. Feinberg, B. Langlais, R. J. Phillips, Timing of the martian dynamo: New constraints for a core field 4.5 and 3.7 Ga ago. *Sci. Adv.* **6**, eaba0513 (2020).

14. S. M. Tikoo, A. J. Evans, Dynamos in the Inner Solar System. *Annu. Rev. Earth Planet. Sci.* **50**, 99–122 (2022).

15. R. K. Bono, J. A. Tarduno, F. Nimmo, R. D. Cottrell, Young inner core inferred from Ediacaran ultra-low geomagnetic field intensity. *Nat. Geosci.* **12**, 143–147 (2019).

16. D. Hemingway, P. Driscoll, *J. Geophys. Res. Planets*, in press, doi:10.1029/2020JE006663.

17. S. C. Stähler, A. Khan, W. Bruce Banerdt, P. Lognonné, D. Giardini, S. Ceylan, M. Drilleau, A. Cecilia Duran, R. F. Garcia, Q. Huang, D. Kim, V. Lekic, H. Samuel, M. Schimmel, N. Schmerr, D. Sollberger, É. Stutzmann, Z. Xu, D. Antonangeli, C. Charalambous, P. M. Davis, J. C. E. Irving, T. Kawamura, M. Knapmeyer, R. Maguire, A. G. Marusiak, M. P. Panning, C. Perrin, A. C. Plesa, A. Rivoldini, C. Schmelzbach, G. Zenhäusern, É. Beucler, J. Clinton, N. Dahmen, M. van Driel, T. Gudkova, A. Horleston, W. Thomas Pike, M. Plasman, S. E. Smrekar, Seismic detection of the martian core. *Science*. **373**, 443–448 (2021).

18. T. Yoshizaki, W. F. McDonough, The composition of Mars. *Geochim. Cosmochim. Acta*. **273**, 137–162 (2020).

19. G. J. Taylor, The bulk composition of Mars. *Chemie der Erde*. **73**, 401–420 (2013).

20. G. Helffrich, Mars core structure—concise review and anticipated insights from insight. *Prog. Earth Planet. Sci.* **4**, 24 (2017).

21. E. Marzotto, W. P. Hsieh, T. Ishii, K. H. Chao, G. J. Golabek, M. Thielmann, E. Ohtani, *Geophys. Res. Lett.*, in press, doi:10.1029/2020GL087607.

22. M. Berrada, R. A. Secco, Review of Electrical Resistivity Measurements and Calculations of Fe and Fe-Alloys Relating to Planetary Cores. *Front. Earth Sci.* **9**, 732289 (2021).

23. F. Wagle, G. Steinle-neumann, N. De Koker, Resistivity saturation in liquid iron-light-element alloys at conditions of planetary cores from first principles computations. *Comptes*

Rendus Geosci. **351**, 154–162 (2019).

24. A. Pommier, Influence of sulfur on the electrical resistivity of a crystallizing core in small terrestrial bodies. *Earth Planet. Sci. Lett.* **496**, 37–46 (2018).

25. G. Manthilake, J. Chantel, J. Monteux, D. Andrault, M. A. Bouhifd, N. Bolfan Casanova, E. Boulard, N. Guignot, A. King, J. P. Itie, Thermal Conductivity of FeS and Its Implications for Mercury's Long-Sustaining Magnetic Field. *J. Geophys. Res. Planets*. **124**, 2359–2368 (2019).

26. J. A. H. Littleton, R. A. Secco, W. Yong, *J. Geophys. Res. Planets*, in press, doi:10.1029/2020JE006793.

27. W.-P. Hsieh, F. Deschamps, T. Okuchi, J.-F. Lin, Effects of iron on the lattice thermal conductivity of Earth's deep mantle and implications for mantle dynamics. *Proc. Natl. Acad. Sci. U. S. A.* **115**, 4099–4104 (2018).

28. W.-P. Hsieh, F. Deschamps, T. Okuchi, J.-F. Lin, Reduced lattice thermal conductivity of Fe-bearing bridgmanite in Earth's deep mantle. *J. Geophys. Res. Solid Earth*. **122**, 4900–4917 (2017).

29. H. Gomi, K. Ohta, K. Hirose, S. Labrosse, R. Caracas, M. J. Verstraete, J. W. Hernlund, The high conductivity of iron and thermal evolution of the Earth ' s core. *Phys. Earth Planet. Inter.* **224**, 88–103 (2013).

30. H. Gomi, K. Hirose, H. Akai, Y. Fei, Electrical resistivity of substitutionally disordered hcp Fe–Si and Fe–Ni alloys: Chemically-induced resistivity saturation in the Earth's core. *Earth Planet. Sci. Lett.* **451**, 51–61 (2016).

31. C. T. Seagle, E. Cottrell, Y. Fei, D. R. Hummer, V. B. Prakapenka, Electrical and thermal transport properties of iron and iron-silicon alloy at high pressure. *Geophys. Res. Lett.* **40**, 5377–5381 (2013).

32. M. Pozzo, C. J. Davies, D. Alfè, Towards reconciling experimental and computational determinations of Earth's core thermal conductivity. *Earth Planet. Sci. Lett.* **584**, 117466 (2022).

33. S. Thompson, T. Komabayashi, H. Breton, S. Suehiro, K. Glazyrin, A. Pakhomova, Y. Ohishi, Compression experiments to 126 GPa and 2500 K and thermal equation of state of Fe3S: Implications for sulphur in the Earth's core. *Earth Planet. Sci. Lett.* **534**, 116080 (2020).

34. S. Urakawa, K. Someya, H. Terasaki, T. Katsura, S. Yokoshi, K. ichi Funakoshi, W. Utsumi, Y. Katayama, Y. ichiro Sueda, T. Irifune, Phase relationships and equations of state for FeS at high pressures temperatures and implications for the internal structure of Mars. *Phys. Earth Planet. Inter.* **143**, 469–479 (2004).

35. Y. Fei, C. Bertka, The Interior of Mars. *Science*. **308**, 1120–1121 (2005).

36. Wendell S. Williams, The Thermal Conductivity of Metallic Ceramics. *JOM*. **50**, 62–66 (1998).

37. Q. Zheng, A. B. Mei, M. Tuteja, D. G. Sangiovanni, L. Hultman, I. Petrov, J. E. Greene, D. G. Cahill, Phonon and electron contributions to the thermal conductivity of v Nx epitaxial layers. *Phys. Rev. Mater.* **1**, 065002 (2017).

38. F. Gronvold, S. Stolen, A. Labban, E. Westrum, Thermodynamics of iron sulfides I. Heat capacity and thermodynamic properties of FesS10 at temperatures from 5 K to 740 K. *J.*

Chem. Thermodyn. **23**, 261–272 (1991).

39. W.-P. Hsieh, E. Marzotto, T. Ishii, L. Dubrovinsky, A. A. Aslandukova, G. Criniti, Y. Tsao, C. Lin, J. Tsuchiya, E. Ohtani, *J. Geophys. Res. Solid Earth*, in press, doi:10.1029/2022jb024556.

40. Y. Xu, T. J. Shankland, S. Linhardt, D. C. Rubie, F. Langenhorst, K. Klasinski, Thermal diffusivity and conductivity of olivine, wadsleyite and ringwoodite to 20 GPa and 1373 K. *Phys. Earth Planet. Inter.* **143**, 321–336 (2004).

41. Y. Zhang, T. Yoshino, A. Yoneda, M. Osako, Effect of iron content on thermal conductivity of olivine with implications for cooling history of rocky planets. *Earth Planet. Sci. Lett.* **519**, 109–119 (2019).

42. S. Suehiro, K. Ohta, K. Hirose, G. Morard, Y. Ohishi, The influence of sulfur on the electrical resistivity of hcp iron: Implications for the core conductivity of Mars and Earth. *Geophys. Res. Lett.* **44**, 8254–8259 (2017).

43. H. Wänke, G. Dreibus, Chemistry and accretion history of Mars. *Phil. Trans. R. Soc. Lond. A.* **349**, 285–293 (1994).

44. A. Jackson, P. W. Livermore, G. Ierley, On Ohmic heating in the Earth's core II : Poloidal magnetic fields obeying Taylor's constraint. *Phys. Earth Planet. Inter.* **187**, 322–327 (2011).

45. H. Samuel, M. D. Ballmer, S. Padovan, N. Tosi, A. Rivoldini, A. C. Plesa, *J. Geophys. Res. Planets*, in press, doi:10.1029/2020JE006613.

46. A. Dewaele, P. Loubeyre, M. Mezouar, Equations of state of six metals above 94 GPa. *Phys. Rev. B.* **70**, 094112 (2004).

47. W.-P. Hsieh, High-pressure thermal conductivity and compressional velocity of NaCl in B1 and B2 phase. *Sci. Rep.* **11**, 21321 (2021).

48. W. P. Hsieh, B. Chen, J. Li, P. Keblinski, D. G. Cahill, Pressure tuning of the thermal conductivity of the layered muscovite crystal. *Phys. Rev. B.* **80**, 180302 (2009).

49. K. Kang, Y. K. Koh, C. Chiritescu, X. Zheng, D. G. Cahill, Two-tint pump-probe measurements using a femtosecond laser oscillator and sharp-edged optical filters. *Rev. Sci. Instrum.* **79**, 114901 (2008).

50. D. G. Cahill, Analysis of heat flow in layered structures for time-domain thermoreflectance. *Rev. Sci. Instrum.* **75**, 5119–5122 (2004).

51. F. Grønvold, E. F. Westrum, C. Chou, Heat capacities and thermodynamic properties of the pyrrhotites FeS and Fe0.877S from 5 to 350°K. *J. Chem. Phys.* **30**, 528–531 (1959).

52. D. G. Cahill, F. Watanabe, Thermal conductivity of isotopically pure and Ge-doped Si epitaxial layers from 300 to 550 K. *Phys. Rev. B.* **70**, 235322 (2004).

53. X. Zheng, D. G. Cahill, P. Krasnochtchekov, R. S. Averback, J. C. Zhao, High-throughput thermal conductivity measurements of nickel solid solutions and the applicability of the Wiedemann-Franz law. *Acta Mater.* **55**, 5177–5185 (2007).

54. D. Breuer, T. Spohn, Viscosity of the Martian mantle and its initial temperature: Constraints from crust formation history and the evolution of the magnetic field. *Planet. Space Sci.* **54**, 153–169 (2006).

55. M. Thiriet, D. Breuer, C. Michaut, A. C. Plesa, Scaling laws of convection for cooling

planets in a stagnant lid regime. *Phys. Earth Planet. Inter.* **286**, 138–153 (2019).

56. S. Greenwood, C. J. Davies, J. E. Mound, On the evolution of thermally stratified layers at the top of Earth's core. *Phys. Earth Planet. Inter.* **318**, 106763 (2021).

Acknowledgments

The troilite sample was provided by Prof. James Connelly at Centre for Star and Planet Formation, GLOBE Institute, University of Copenhagen. The Fe_3S samples were synthesized using joint-use facilities of the Institute for Planetary Materials, Okayama University. We are very grateful to Prof. Christopher J. Davies at University of Leeds, UK, for performing numerical simulations. We also thank Dr. Yoshiyuki Iizuka at Academia Sinica for his help with the EPMA analysis.

Funding:

Academia Sinica grant AS-IA-111-M02 (WPH)
National Science and Technology Council of Taiwan, Republic of China grant 110-2628-M-001-001-MY3 (WPH)
Foundation for the Advancement of Outstanding Scholarship, Taiwan (WPH)
Geophysics Program of the National Science Foundation, USA, grant EAR-1901801 (JFL)

Author contributions:

Conceptualization: WPH, FD, JFL
Methodology: WPH
Source: TY
Investigation: WPH, YCT
Supervision: WPH, FD
Writing—original draft: WPH, FD
Writing—review & editing: WPH, FD, YCT, TY, JFL

Competing interests:

Authors declare that they have no competing interests.

Data and materials availability:

All experimental data are available in https://doi.org/10.5281/zenodo.7953943

Figures and Tables

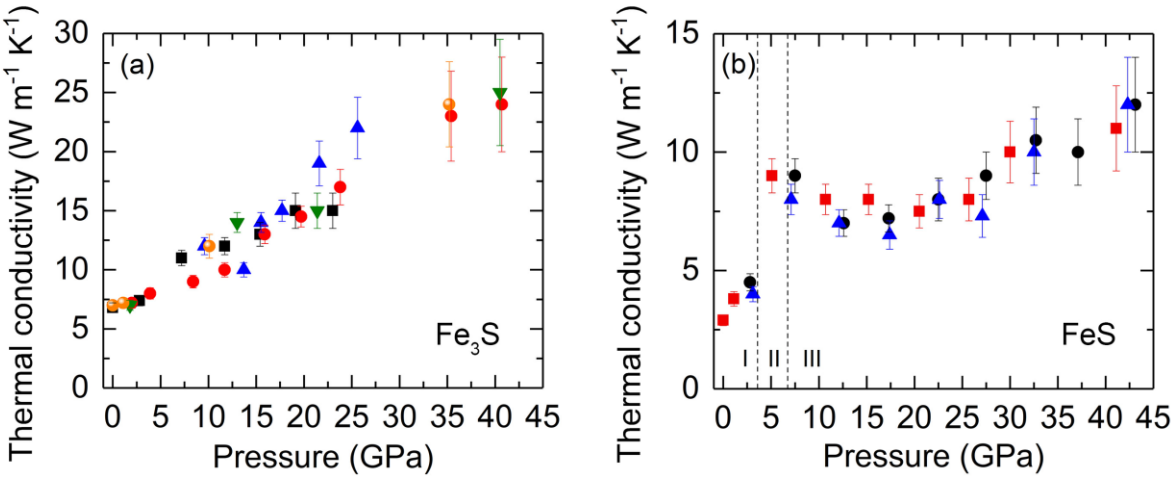

Figure 1. Thermal conductivity of (a) Fe_3S and (b) FeS at high pressure and room temperature. For both compositions, several runs of measurements show consistent results, where each run is represented by a symbol set. Vertical bars show uncertainties which are mainly from the error propagations in spectral modelling analysis: <10% before 20 GPa and ~10–17% at 20–40 GPa. Note that at ~40 GPa, the thermal conductivity of FeS is only half of the Fe_3S, indicating a strong reduction by the sulfur impurity. For FeS in (b), the two vertical dashed lines represent the phase transition pressures for FeS I-II at ~3.4 GPa and II-III at ~6.7 GPa (*34*), respectively.

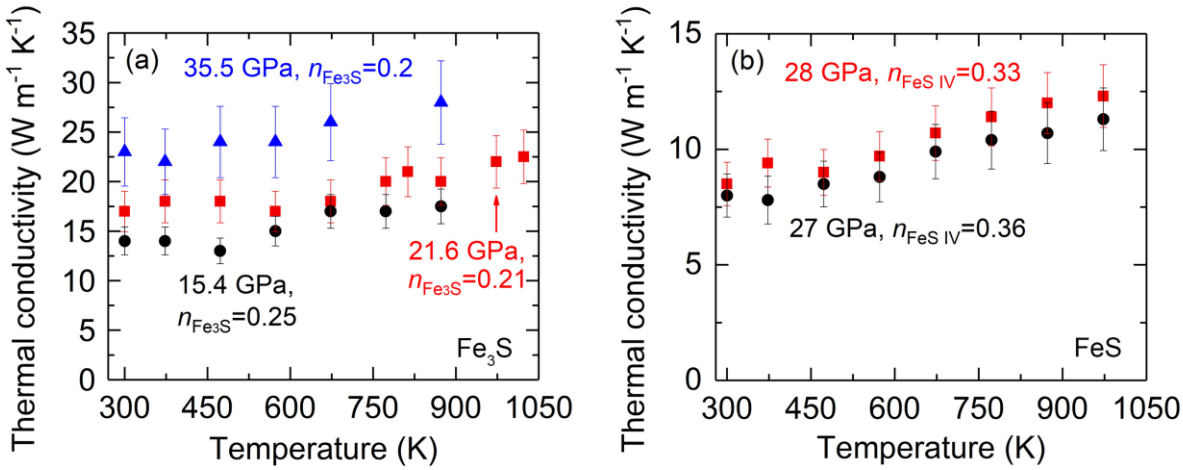

Figure 2. Temperature dependence of the thermal conductivity of Fe-S alloys at high pressures. Assuming the thermal conductivity scales with T^n, the n for (a) Fe_3S decreases from 0.25(±0.07) at 15.4 GPa to 0.2(±0.04) at 35.5 GPa. (b) The FeS IV phase (at T > 730 K) has a larger temperature exponent n (0.33 at 28 GPa and 0.36 at 27 GPa) than that of Fe_3S (0.2–0.25) at relevant Martian core's pressures. Vertical bars represent analysis uncertainties of the data at ~10–15%.

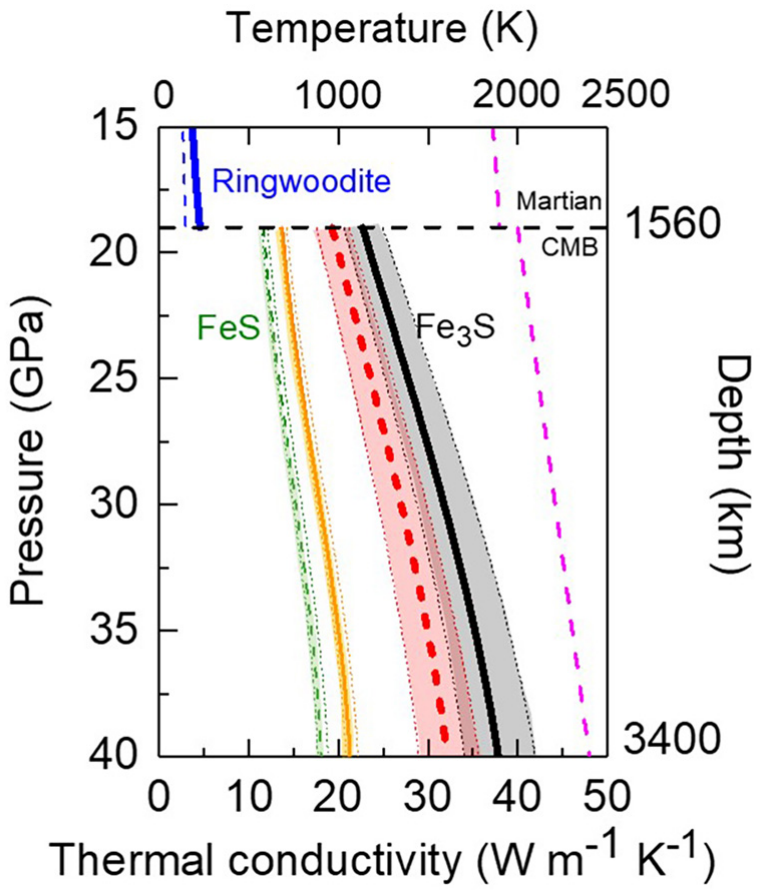

Figure 3. Modeled thermal conductivity profile in Martian mantle and core. Assuming the Martian liquid core is majorly composed of Fe_3S (*20*), its thermal conductivity (red dashed curve) spans from ~19 W m^{-1} K^{-1} at the top to ~32 W m^{-1} K^{-1} at the center. The thermal conductivity of FeS in solid (orange curve) and liquid (green dashed curve) phase, respectively, are plotted for comparison. Note that the thermal conductivity of liquid FeS was estimated by a 15% reduction from that of the FeS V phase, which was assumed to have the same temperature dependence as FeS IV phase. The shaded areas represent the uncertainty ranges considering the small variation of the temperature exponent *n*. The solid and dashed blue curves are the thermal conductivity of ringwoodite with 0.11 wt% (dry) and 1.73 wt% (hydrous) water (*21*), respectively, along an estimated Martian mantle areotherm (magenta dashed curve with the temperature scale at the top axis) taken from Ref (*35*). A ~4 to 6-fold discontinuity in the thermal conductivity across the Martian CMB (liquid Fe_3S vs. ringwoodite) is estimated.

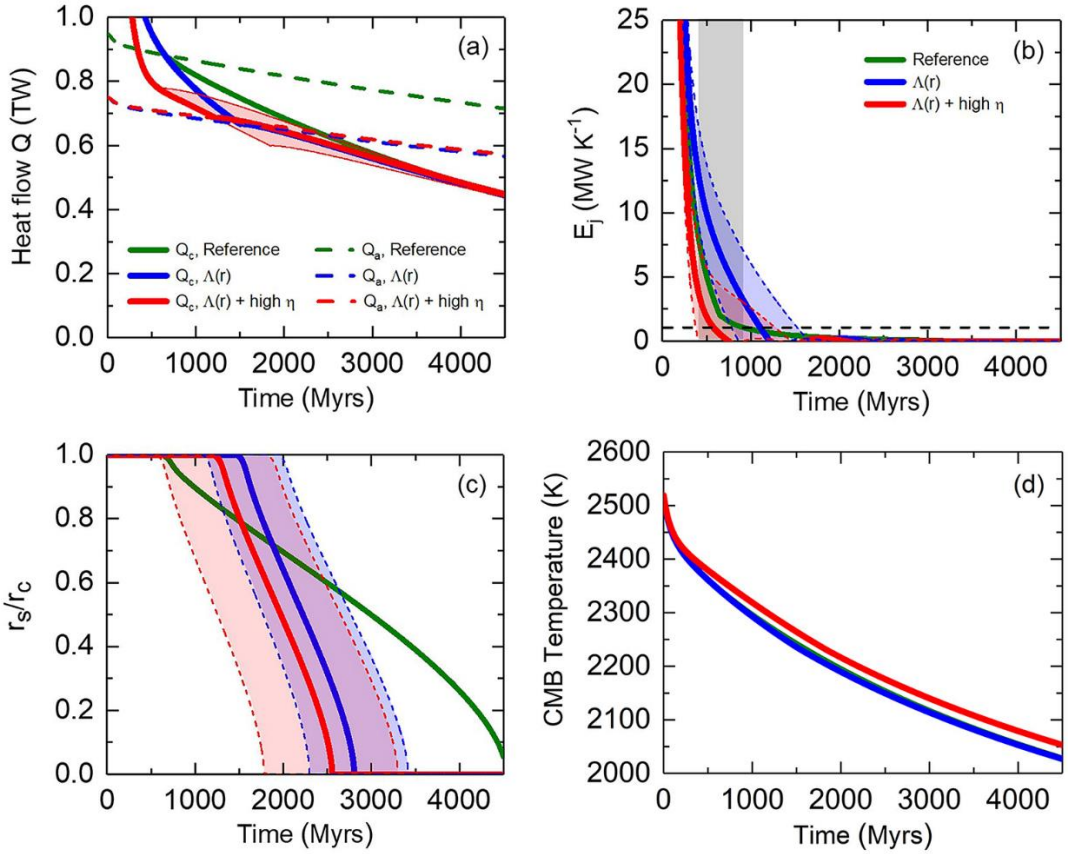

Figure 4. Thermal evolution scenarios of the Martian core. Three scenarios are described in the text in detail. (a) Heat flow across the Martian CMB, Q_c (solid curves), vs. isentropic heat flow, Q_a (dashed curves). (b) Entropy due to the Ohmic dissipation, E_j. The dynamo will stop as $E_j < 1.0$ MW K^{-1} (horizontal dashed line), which occurs around the transition from super- to sub-isentropic heat flow, i.e., Q_c being slightly higher or lower than Q_a. The grey zone indicates the range of cessation time of dynamo based on remnant crustal magnetism. (c) Ratio of the radius of the base of thermal stratification layer (r_s) to the radius of the core (r_c). Thermal stratification starts when Q_c becomes lower than Q_a. The shaded region in all the figures represents the uncertainty of each curve. (d) Temperature at the Martian CMB, where the green and blue curves are close to each other.

Table 1. Recent experimental and computational results of electrical resistivity ρ and thermal conductivity Λ of Fe-S alloys at Martian CMB conditions

Composition	ρ ($\mu\Omega$ cm)	Λ (W m^{-1} K^{-1})	Method	Reference
solid Fe-16wt%S	NA	~22.7	DTCM+E	This study
solid Fe-36wt%S	NA	~13.7	DTCM+E	This study
solid Fe-14.2wt%S	~100	~46*	ERM+E	(*42*)
liquid Fe-16.1wt%S	~107	~43.3*	C	(*23*)
liquid Fe-7.6wt%S	~88	~52.7*	C	(*23*)

*Thermal conductivity was inferred from electrical resistivity via WF law with ideal Lorenz number.

Method: DTCM: direct thermal conductivity measurement; E: extrapolation; ERM: electrical resistivity measurement; C: calculation

NA: not applicable

Science Advances
AAAS

Supplementary Materials for

A thermally-conductive Martian core and implications for its dynamo cessation

Wen-Pin Hsieh* *et al.*

*Corresponding author. Email: wphsieh@earth.sinica.edu.tw

This PDF file includes:

Figs. S1 and S2
Table S1

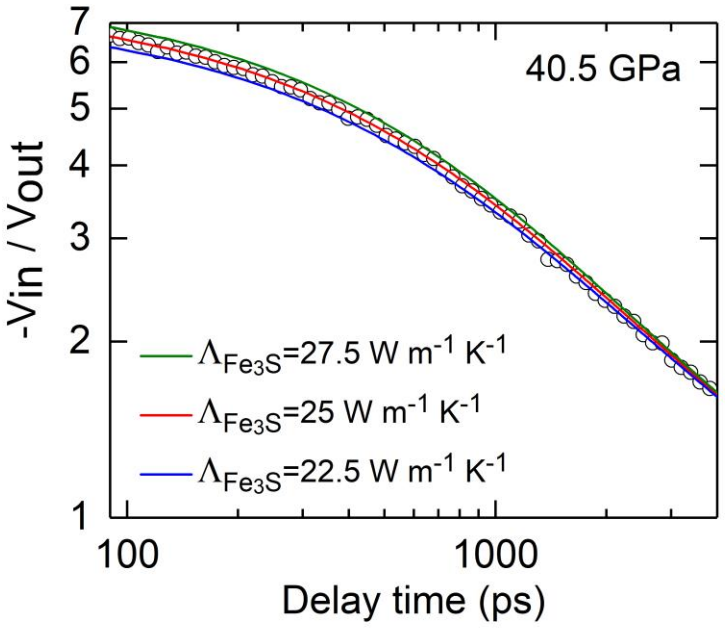

Fig. S1. Example TDTR spectrum (open circles) along with thermal model calculations (color solid curves) for Fe_3S at 40.5 GPa. Using the input parameters listed in Table S1, Λ_{Fe3S}=25 W m^{-1} K^{-1} (red curve) enables a best-fit to the TDTR data. The spectrum ratio $-V_{in}/V_{out}$ is most sensitive to the sample's thermal conductivity at delay times of few hundred picoseconds (ps), see Ref (*48, 49*) for details. A test variation of 10% in Λ_{Fe3S}, i.e., green and blue curves, results in a clear deviation from the data. Such high sensitivity indicates our thermal model fitting and the derived Λ_{Fe3S} are precise and reliable based on the high-quality data.

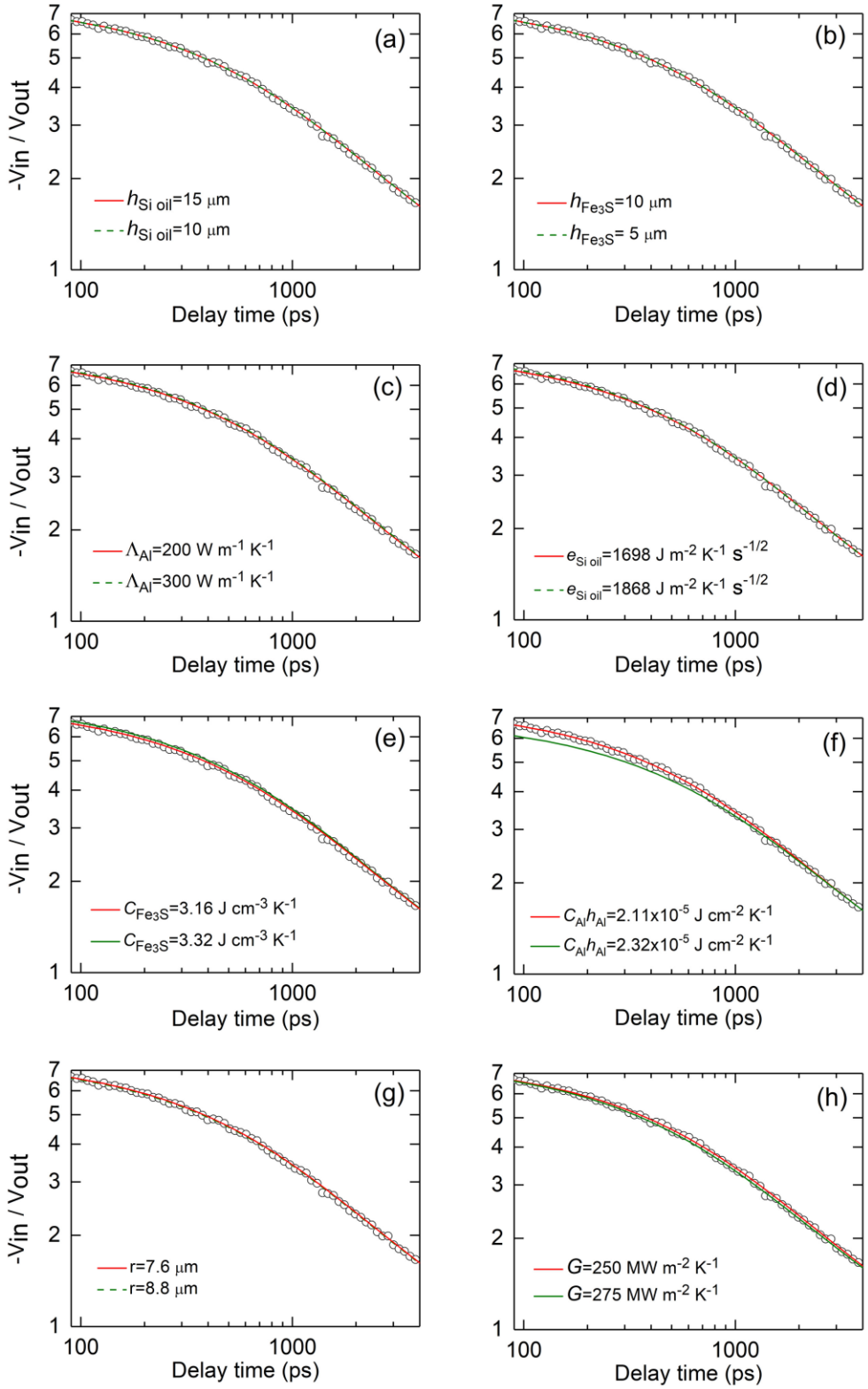

Fig. S2. Sensitivity tests of the thermal model to input parameters for Fe_3S at 40.5 GPa. Thermal conductivity of Fe_3S, Λ_{Fe3S}, is fixed at 25 W m^{-1} K^{-1}, as shown in Fig. S1. (a) and (b) Changes in

the thicknesses of silicone oil ($h_{\text{Si oil}}$) and Fe_3S (h_{Fe3S}) by 33% and 50%, respectively, have essentially no influence on the model calculations, i.e., the derived Λ_{Fe3S} is not affected by the uncertainties in the $h_{\text{Si oil}}$ and h_{Fe3S}. (c) Large uncertainty in the high thermal conductivity of Al film has very minor effect on the Λ_{Fe3S}. (d) If the thermal effusivity of the pressure medium silicone oil, $e=(\Lambda_{Si}C_{Si})^{1/2}$, has 10% uncertainty, it requires the Λ_{Fe3S} to decrease to 24.5 W m^{-1} K^{-1} to re-fit the data, i.e., producing 2% uncertainty. (e) If the volumetric heat capacity of Fe_3S, C_{Fe3S}, is 5%, a Λ_{Fe3S}=24.3 W m^{-1} K^{-1} can re-fit the data, i.e., propagating 3% uncertainty. (f) In our analysis, the major uncertainty is from the uncertainty in the heat capacity of Al film per unit area, i.e., product of volumetric heat capacity and thickness, $C_{Al}\,h_{Al}$. This is because the ratio $-V_{in}/V_{out}$ at few hundred picosecond delay time scales inversely with the $C_{Al}\,h_{Al}$ (*49*). If there is a 10% uncertainty, it requires ~16% change in the Λ_{Fe3S} to fit the data. (g) Changing the laser spot size by 15% does not influence the model calculation, i.e., its uncertainty has essentially no effect on the Λ_{Fe3S}. (h) 10% variation in the thermal conductance of Al/Fe_3S and Al/silicone oil interfaces, *G*, lead to a very minor change in the model calculation, propagating only ~4% uncertainty in the Λ_{Fe3S}.

Table S1. Input parameters in the thermal model for Fe_3S at 40.5 GPa and 300 K in TDTR measurements

P (GPa)	C_{Fe3S} (J cm^{-3} K^{-1})	C_{Al} (J cm^{-3} K^{-1})	h_{Al} (nm)*	$e=(\Lambda_{Si}C_{Si})^{1/2}$ (J m^{-2} K^{-1} s$^{-1/2}$)	r (μm)	$h_{Fe3S/Si\ oil}$ (μm)	Λ_{Al} (W m^{-1} K^{-1})	G (MW m^{-2} K^{-1})
40.5	3.16	2.68	79.0	2260	7.6	10/15	200	250

*In this experimental run, the Al thickness at ambient pressure is 90 nm.
C_{Fe3S}: Fe_3S heat capacity, C_{Al}: Al heat capacity, h_{Al}: Al thickness, e: silicone oil thermal effusivity, r: laser spot size, h_{Fe3S}: Fe_3S thickness, $h_{Si\ oil}$: silicone oil thickness, Λ_{Al}: Al thermal conductivity, G: thermal conductance of Al/Fe_3S and Al/silicone oil interfaces.